PCCP

Accepted Manuscript

ROYAL SOCIETY OF CHEMISTRY

www.rsc.org/pccp

Advanced oxygen reduction reaction catalyst based on nitrogen and sulfur co-doped graphene in alkaline medium

Yongfeng Li,[a] Meng Li,[a] Liqing Jiang,[a] Lin Lin,[a] Lili Cui,[a] Xingquan He [a,*]

[a]*Department of Chemistry and Chemical Engineering, Changchun University of Science and Technology, Changchun 130022, P. R. China.*

[*]Corresponding author.Tel.+86-431-85583430

E-mail address: hexingquan@hotmail.com (X. Q. He)

Abstract

A novel nitrogen and sulfur co-doped graphene (N-S-G) catalyst for oxygen reduction reaction (ORR) has been prepared by pyrolysing graphite oxide and poly[3-amino-5-mercapto-1,2,4-triazole] (PAMTa) composite. The atomic percentage of nitrogen and sulfur for the prepared N-S-G can be adjusted by controlling pyrolysis temperature. Furthermore, the catalyst pyrolysed at 1000 ℃, denoted N-S-G 1000, exhibits the highest catalytic activity for ORR, which displays the highest content of graphitic-N and thiophene-S in all pyrolysed samples. And the electrocatalytic performance of N-S-G 1000 is significantly better than that of PAMTa and reduced graphite oxide composite. Remarkably, the N-S-G 1000 catalyst is comparable with Pt/C in terms of the onset potential and half-wave potential and displays larger kinetic limiting current density, better methanol tolerance and stability than Pt/C for ORR in alkaline medium.

1. Introduction

The oxygen reduction reaction (ORR) plays a decisive role in adjusting the performance of fuel cells.[1] The ORR is very sluggish in nature and therefore needs the exclusive of highly efficient catalysts.[2] Nowadays, platinum (Pt)- based materials or Pt is regarded as the best ORR catalyst for commercialized fuel cells. However, the high-cost, intolerance to the crossover effect and instability of Pt has already become the main technical bottleneck of fuel cells.[3] In this context, as replacements for these Pt-based materials, various non-precious-metal and metal-free catalysts, which are of low cost, excellent electrocatalytic activity and good stability, have attracted much attention.[4-11]Although both theoretical calculations and experiments have been extensively studied to find an ideal cathode catalyst, the results are far from satisfactory owing to the limited reaction rate and environmental hazards.[12]

In recent years, carbon-based (carbon nanotubes and graphene) materials with unique electronic structures have attracted far-ranging attention as candidates for electrochemical applications in super capacitor, sensors, fuel cells and metal-air batteries.[13-21] Graphene, a single layer carbon atoms covalently bonded into a hexagonal lattice, is greatly important and desirable for electrochemical processes owing to its excellent electrical properties and theoretically ultrahigh specific surface area.[22] It is a promising matrix material for catalysts of the ORR. Remarkably, artificial doping of graphene with heteroatoms, such as B, N, S, P or F,

can effectively change its electronic properties and chemical reactivity, thus making doped graphene possess excellent catalytic activity towards ORR.[1, 12, 13-33]

Recently, metal-free N-doped graphene (N-G) has been reported, successful regulation ways of doping behavior of N-G with different kinds of nitrogen source can fabricate high-performance catalysts for ORR.[23, 34-37] The superior performance of N-G makes it a promising ORR catalyst for application in fuel cells and metal-air batteries. Besides, sulfur-doped graphene (S-G) also shows high activity for ORR.[25, 29] However, the ORR mechanisms of these doped materials are still not completely clear.[38] It is generally considered that the heteroatoms doping should easily change materials intrinsically, modify electronic properties and tailor surface chemistry of host materials.[39] Moreover, previous reports have demonstrated that graphitic-N and pyridinic-N are the key catalytic active sites for ORR in N-G,[23] and thiophene-S plays a decisive role in sulfur-doped graphene.[25] The content of these main active sites can be controlled by adjusting the pyrolysis temperature and the structure of the dopant.[18, 29] To further improve the performance of N-G and S-G, the nitrogen and sulfur co-doped graphene (N-S-G) has been researched as well.[40] Indeed, its catalytic activity for ORR is better than N-G and S-G alone due to the synergistic effect caused by doping N and S.[41]

3-amino-5-mercapto-1,2,4-triazole (AMTa) is a polymerizable monomer with high nitrogen and sulfur content, and conjugated structure. Herein, using AMTa as a monomer, poly[3-amino-5-mercapto-1,2,4-triazole] (PAMTa) was synthesized via a solution polymerization method and in situ coated on GO surface. A novel N-S-G

catalyst was prepared by pyrolysing PATMa and GO composite (PAMTa/GO). The catalyst pyrolysed at 1000 ℃ (N-S-G 1000) possesses excellent ORR performance compared with commercial Pt/C catalyst. And the electrocatalytic performance of N-S-G 1000 is significantly better than that of PAMTa and reduced graphite oxide (rGO) composite (PAMTa/rGO).

2. Experimental

2.1. Chemicals

Natural flake graphite powder was bought from Beijing Chemical Company (China). 3-amino-5-mercapto-1,2,4-triazole and 3-amino-1,2,4-triazole were obtained from Aladdin. Pt/C (20 wt. % Pt on VulcanXC-72) was purchased from Alfa Aesar. All other reagents were analytical grade and used without further purification, and all solutions used in electrochemical experiments were prepared with ultrapure water (18.2 MΩ cm).

2.2. Material synthesis

GO was prepared from natural flaked graphite using modified Hummers method.[32] PAMTa/GO composite was fabricated via a solution polymerization method. Simply, 200 mg GO was dispersed in 40 mL water by ultrasonication. Then, concentrated HCl (37 wt. %) was added to the GO suspension to form a 1 M HCl solution. After that, 200 mg AMTa monomer and 5 mL of 1 M HCl containing 588.7 mg $(NH_4)_2S_2O_8$ (APS) were added into the above GO suspension. The mixture was stirred at 30 ℃ for 24 h. The obtained PAMTa/GO composite was collected by

vacuum filtration and washed with deionized water until the filtrate was neutral, then dried at 35 ℃ over night in the vacuum oven.

The N-S-G catalysts were prepared by pyrolysing PAMTa/GO composite at 600, 700, 850 and 1000 ℃ for 1 h in an Ar atmosphere, abbreviated as N-S-G 600, N-S-G 700, N-S-G 850 and N-S-G 1000, respectively. The heating rate is 10 ℃ min^{-1}. N-doped graphene pyrolysed at 1000 ℃ (N-G 1000) was synthesized using3-amino-1,2,4-triazole as the dopant with the same synthesis routes of N-S-G 1000. The synthesis routes of N-S-G are illustrated in Scheme 1.

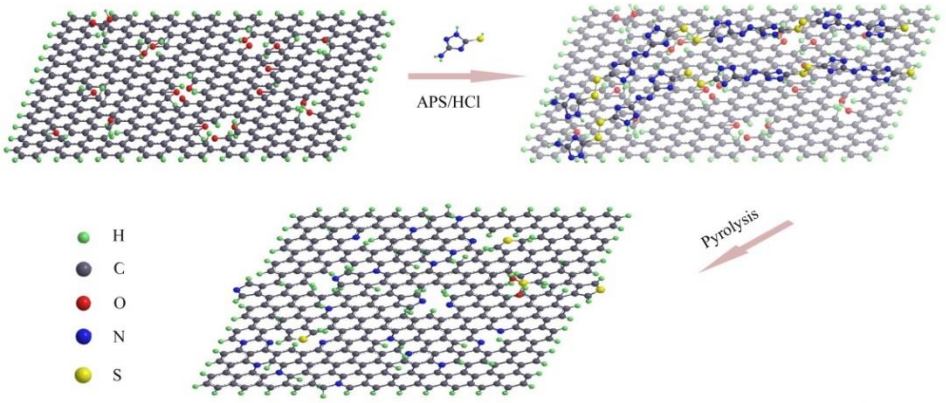

Scheme 1. Schematic illustration of the synthesis route of N-S-G with GO and AMTa.

To prepare PAMTa/rGO composite, 2.5 mL hydrazine hydrate was added to a 50 mL (1 mg mL^{-1}) PAMTa/GO suspension with stirring at 90 ℃ for 24 h. Then the composite was collected by vacuum filtration and washed by centrifugation with deionized water.

2.3. Characterization

The morphology and structure of samples were observed using transmission electron microscopy (TEM, JEOL-2010 transmission electron microscope operating at 200 kV). Atomic force microscopy (AFM) images were recorded in the tapping

mode with a Nanoscope III a scanning probe microscope from Digital Instruments under ambient conditions. X-ray diffractometer (XRD, RIGAK, D/MAX2550VB/PC, Japan) was used to determine the crystal structure. Raman spectra analysis was carried out on a TriVistaTM555CRS Raman spectrometer at 785 nm. X-ray photoelectron spectroscopy (XPS) analysis was taken on an ESCLAB 250 spectrometer with a monochromatized Al Kα X-ray source (1486.6 eV photons) to character surface chemical composition and the valence state.

2.4. Electrochemical measurements

Prior to modification, the glassy carbon (GC) electrode was polished to be smooth with 1.0, 0.3 and 0.05 μm α-Al_2O_3 powder slurry, then treated by ultrasonication with absolute ethanol and deionized water in turn. The N-S-G was dispersed into ethanol by ultrasonication at a concentration of around 1 mg mL^{-1}. Afterwards, a certain amount of the catalyst ink was dropped onto the freshly polished electrode surface. Finally, 5 μL of 0.5 wt. % Nafion solution (in ethanol) was coated onto the electrode surface to protect catalyst film. The catalyst loading per area was kept to 566 μg cm^{-2}. The same amount of PAMTa/rGO or Pt/C catalyst was also loaded onto the GC electrode for comparison.

Cyclic voltammetry (CV) was performed on a CHI 660D electrochemical workstation (Shanghai CHENHUA company) in a conventional three-electrode cell using the coated GC electrode (d = 3 mm) as the working electrode, a platinum wire as the counter electrode, and a saturated calomel electrode (SCE) as reference at a scan rate of 100 mVs^{-1} in a N_2- or O_2-saturated 0.1 M NaOH solution. The rotating

disk electrode (RDE, d = 5 mm), current-time chronoamperometric response (i-t) and rotating ring disk electrode (RRDE, d_{disk} = 5.61 mm) were operated on a Pine Instrument Company AF-MSRCE modulator speed rotator on a CHI660E electrochemical workstation (CH Instruments, USA) with a standard three-electrode system at a scan rate of 10 mV s^{-1} in an O_2-saturated 0.1 M NaOH solution. The polarization of Pt ring was regulated at 0.1 V *vs*. SCE to detect the production of HO_2^- in a RRDE configuration. The collection efficiency of platinum ring is 37 %.

3. Results and discussion

3.1. Structure and composition characterization of N-S-G

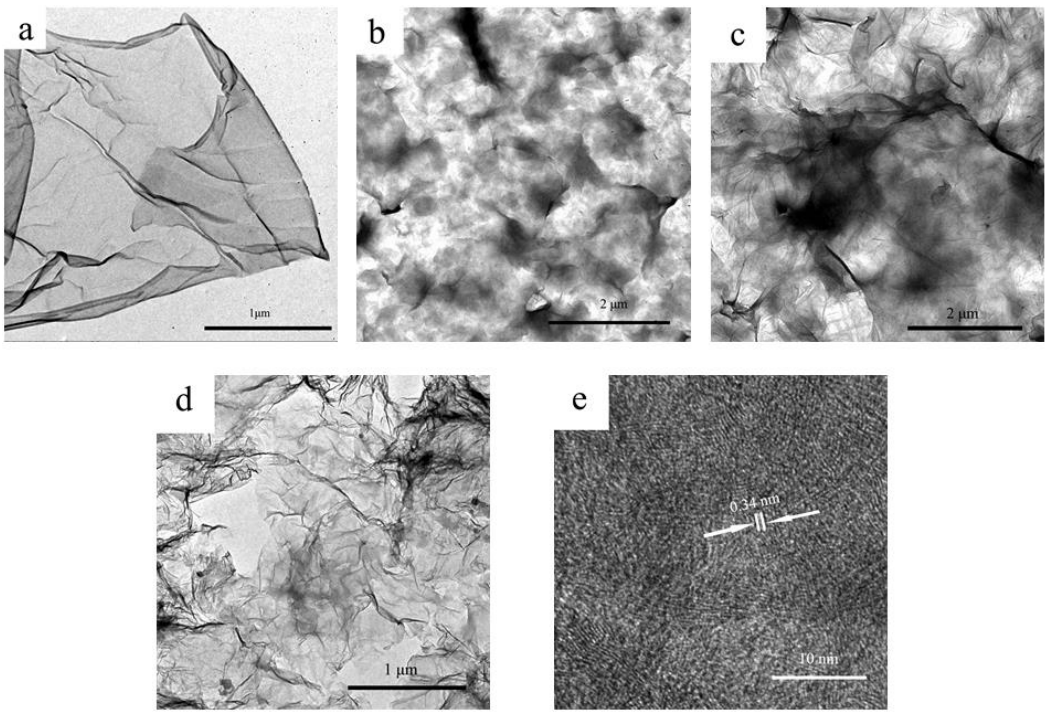

Figure 1. TEM images of (a) GO, (b) PAMTa/GO, (c) PAMTa/rGO and (d) N-S-G 1000, (e) HRTEM image of N-S-G 1000.

The morphology and structure of GO, PAMTa/GO, PAMTa/rGO and N-S-G1000 was investigated via TEM. In Fig. 1a, the GO presents a wrinkle laminar structure. For PAMTa/GO, a thin layer of polymer coated on the surface of GO is distinctly observed, as shown in Fig. 1b. The PAMTa layer can still be found on rGO after reduction of PAMTa/GO with hydrazine hydrate (Fig. 1c). After pyrolysing under 1000 ℃ (Fig. 1d), however, the PAMTa layer disappears. And the formed N-S-G displays more wrinkle structure in comparison with GO, which should provide more active sites and increase specific surface area of graphene.[43] In the high-resolution TEM image of N-S-G 1000 (Fig. 1e), the lattice spacing is around 0.34 nm, which is consistent with the separation of (002) layers of hexagonal graphite.[1] Further structural details of N-S-G 1000 are also evident in AFM. The N-S-G 1000 displays a wrinkle nanosheets structure and there exists obvious aggregation, as shown in Supplementary Fig. S1. Flattened N-S-G nanosheets with an average thickness of about 3.0 nm can be observed, corresponding to less than ten single graphene layers by considering the theoretical thickness of a single-layer graphene (~0.34 nm).

To confirm the reduction of GO during pyrolysis process and the resulting structures, X-ray diffraction tests were conducted. As shown in Supplementary Fig. S2, the XRD pattern of N-S-G 1000 presents a broad peak at ~26.4 º, corresponding to an inter-layer spacing of 0.340 nm that is close to 0.335 nm for graphite, which is similar to that of the HRTEM result. The diffraction peak of GO indexed to (002) shifts negatively to ~11.2 º, which corresponds to a layered structure with a basal

spacing of 0.79 nm.[35] These results indicate that pyrolysis treatment of GO will partially restore the graphitic crystal structure owing to the reduction effect of high temperature and nitrogen/sulfur co-doping.

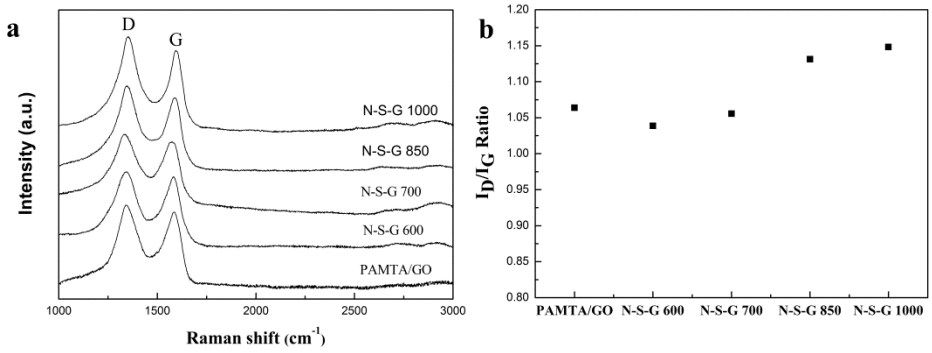

Figure 2. (a) Raman spectra of PAMTa/GO, N-S-G 600, N-S-G 700, N-S-G 850 and N-S-G 1000 (b) The corresponding I_D/I_G ratio.

In an effort to better explore the structure and composition of as-prepared samples, Raman spectroscopy and X-ray photoelectron spectroscopy (XPS) were utilized. Fig. 2a depicts the Raman spectroscopy of PAMTa/GO, N-S-G 600, N-S-G 700, N-S-G 850 and N-S-G 1000. The ratio of I_D/I_G for different samples is shown in Fig. 2b. The I_D/I_G ratio of N-S-G 600 and N-S-G 700 is smaller than that of PAMTa/GO, which should be attributed to the recovery of partly conjugated structure of graphene through thermal reduction. While further increasing pyrolysis temperature, the I_D/I_G ratio of N-S-G becomes larger. This phenomenon is probably due to most of the epoxy and hydroxyl groups begin to decompose and give rise to the in-plane C=C crack at higher temperature.[23]

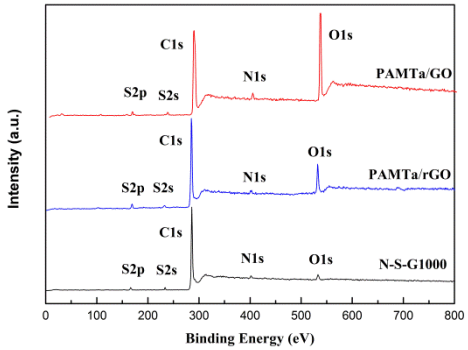

Figure 3.XPS broad scan spectra of PAMTa/GO, PAMTa/rGO and N-S-G 1000.

Fig. 3 presents the XPS broad scan spectra of PAMTa/GO, PAMTa/rGO and N-S-G 1000. Nitrogen and sulfur signals can be clearly observed, demonstrating that PAMTa was loaded on GO and rGO, and both N and S were successfully incorporated into graphene layers after pyrolysing.

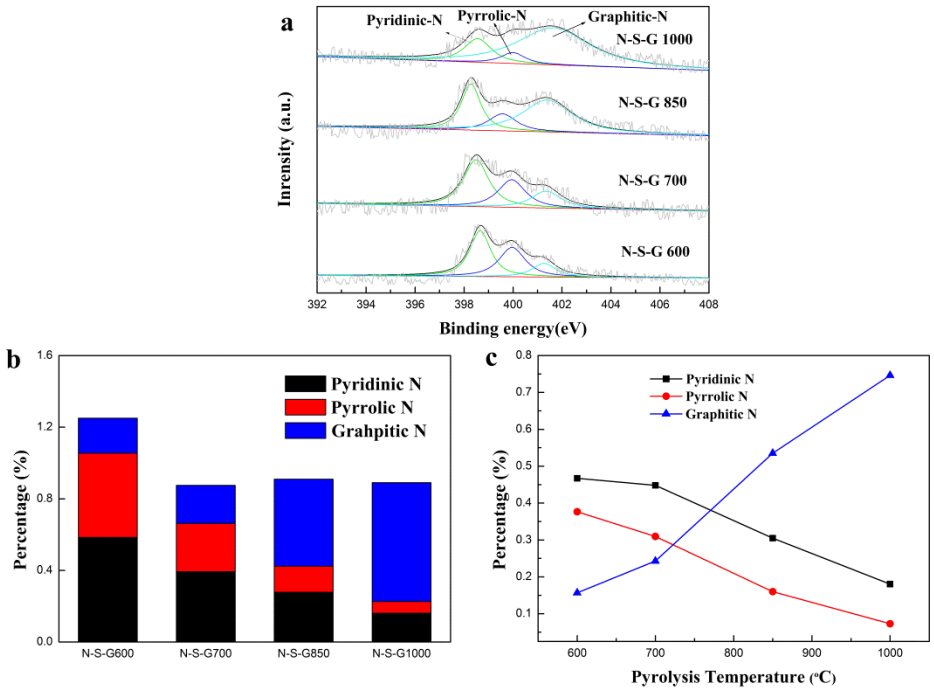

Figure 4. (a) High-resolution N1s XPS spectra of N-S-G pyrolysed at different pyrolysis temperature. (b) The atomic percentage of three nitrogen species in N-S-G sheets pyrolysed at

different pyrolysis temperature. (c) The percentage of three nitrogen species in nitrogen pyrolysed at different pyrolysis temperature.

Figure S3 presents the XPS broad scan spectrum and the high-resolution N1s spectrum of N-G 1000. The nitrogen signals can be clearly seen in the broad scan spectrum, which indicates that N was successfully incorporated into graphene layers after pyrolysing at 1000 ℃. The high-resolution N1s spectra of N-G 1000 can be resolved into three different peaks centered at 398.27, 399.40, 401.22 eV, corresponding to pyridinic-N, pyrrolic-N and graphitic-N, respectively.

To probe the chemical state of nitrogen and sulfur in co-doped graphene sheets, the high resolution N1s and S2p peaks of N-S-G were analysed. As shown in Fig. 4a and b, all N-S-G samples exhibit obvious N1s signals, and the total content of N in N-S-G is in the range of 0.89-1.25 %. The complex N1s peaks deconvolution further suggests that there are three components in N-S-G centered at 398.3, 400, 401.3 eV, corresponding to pyridinic-N, pyrrolic-N and graphitic-N, respectively (Fig. 4a). Remarkably, the area of these three peaks significantly changes with increasing pyrolysis temperature, which suggests that different amounts of N bonding configurations were formed during pyrolysing at various temperatures. As shown in Fig. 4b, when the pyrolysis temperature is between 700 and 1000 ℃, the total content of N in N-S-G remains relatively unchanged. Furthermore, with the increase of pyrolysis temperature from 600 to 1000 ℃, graphitic-N becomes dominant, while the content of pyridinic-N and pyrrolic-N becomes lower (Fig. 4c). The results imply that high pyrolysis temperature does faintly influence the total

content of nitrogen, but it can promote the formation of graphitic-N and prohibit the generation of pyridinic-N and pyrrolic-N.

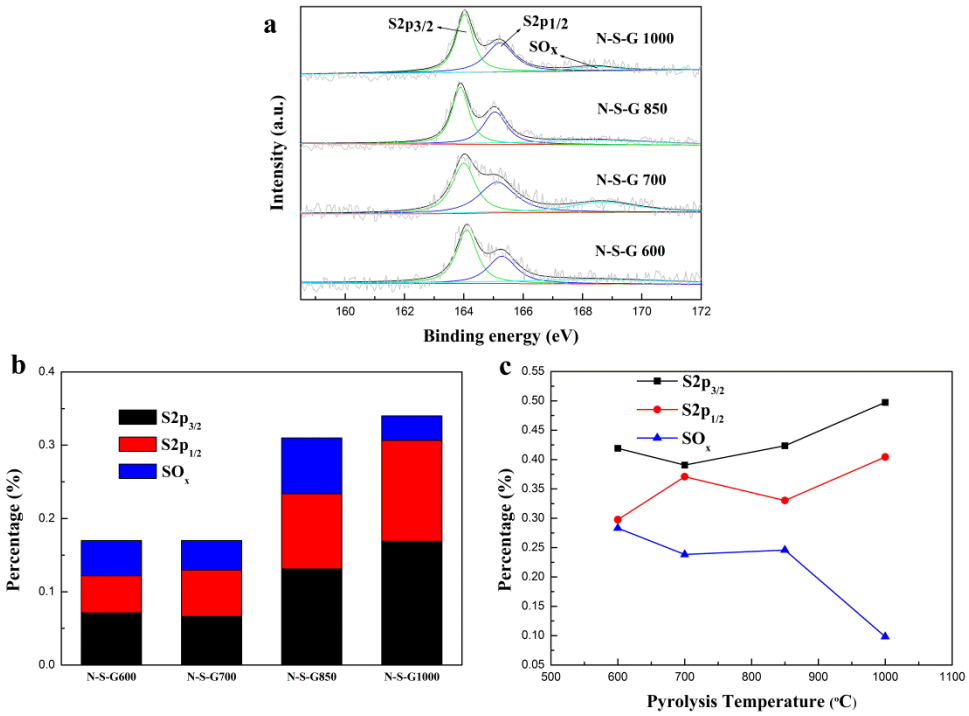

Figure 5. (a) High-resolution S2p XPS spectra of N-S-G pyrolysed at different pyrolysis temperature. (b) The atomic percentage of three sulfur species in N-S-G sheets pyrolysed at different pyrolysis temperature. (c) The percentage of three sulfur species in sulfur pyrolysed at different pyrolysis temperature.

The high-resolution S2p XPS spectra of N-S-G can be resolved into three different peaks (Fig. 5a). The two peaks at binding energies of around 163.9 and 165 eV can be identified as the spin-orbit coupling positions of $2p_{3/2}$ and $2p_{1/2}$ for thiophene-S, and the third peak at around 168.5 eV corresponds to SO_x moieties, which is inoperative for ORR.[44] Thiol group (-SH) signals at around 162 eV can not be detected in the S2p XPS spectra, which means that all the sulfur atoms were embedded in the edge and defect of graphene layers in the form of thiophene-S and

SO_x, without forming thiol groups on the surface of graphene. In Fig. 5b, the overall content of sulfur in N-S-G is in the range of 0.17-0.34 %, with the highest content for N-S-G 1000. It is seen from Fig. 5c, the content of thiophene-S increases with the increase of pyrolysis temperature, while the formation of SO_x is hindered, indicating the lower stability of SO_x at higher temperature.

The above-mentioned results suggest that high pyrolysis temperature is beneficial for both nitrogen and sulfur to form high-effective activesites for ORR.

The high-resolution spectra of C1s in N-S-G 1000 and GO (Supplementary Figure S4) can be deconvoluted into several single peaks. There are two obvious peaks at binding energies near 285 and287 eV for GO, which can be assigned to graphitic C=C (C–C) and oxygen-containing functional groups. The deconvolution of the C (1s) peak of GO exhibits five peaks centered at binding energies of 284.58, 285.26, 286.79, 287.43 and 288.61 eV, which can be assigned to the C-H (C-C, C=C), C-OH, epoxide (C-O-C), C=O (carbonyl C) and O=C-OH (carboxylate C) functional groups, respectively.[8] There is only one obvious peak at binding energies near 285 eV for N-S-G 1000, which can be deconvoluted into four single peaks, corresponding to C-S-C (283.90 eV) , C-H (C-C, C=C, 284.68 eV), C-OH (285.40 eV) and C-N-C (287.20 eV).[8] It is obvious that most of oxygen-containing groups have been removed from the carbon atoms under 1000 ℃ and Ar protection. The above results clearly reveal that the conjugated structure of the graphene sheets was partly restored and heteroatoms (N and S) were successfully doped into the graphene framework.[25]

3.2. Electrocatalytic activity of N-S-G towards ORR in alkaline medium

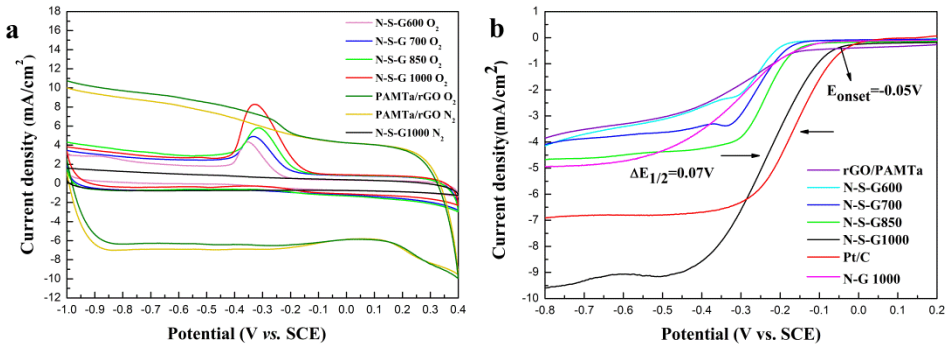

Figure 6. (a) CVs of N-S-G 1000 and PAMTa/rGO in N_2- or O_2- saturated 0.1 M NaOH at a scan rate of 100 mV $s^{-1}$and CVs of N-S-G 600, N-S-G 700,N-S-G 850in O_2-saturated 0.1 M NaOH at a scan rate of 100 mV s^{-1}. (b) LSVs of PAMTa/rGO, N-S-G 600, N-S-G 700, N-S-G 850, N-S-G 1000, N-G 1000 and Pt/C in O_2-saturated 0.1 M NaOH at a scan rate of 10 mV s^{-1} with a rotation speed of 2000 rpm, respectively.

The ORR catalytic activity of the samples was firstly examined by CV in a 0.1 M NaOH solution saturated with either nitrogen or oxygen. As shown in Fig. 6a, featureless voltammetric current on N-S-G 1000can be observed within the potential range of -1.0 to +0.4 V *vs.* SCE in N_2-saturated 0.1 M NaOH solution. The CV curve of PAMTa/rGO displays a rhombus in N_2-saturated 0.1 M NaOH solution. After the solution was saturated with O_2, there is an unconspicuous peak appeared at around -0.26 V *vs.* SCE for ORR. However, notable ORR peaks on all pyrolysed samples were observed, and the peak current increases obviously with increasing pyrolysis temperature. N-S-G 1000 displays more positive peak potential and the maximum peak current. These results suggest pyrolysis temperature can remarkably

influence the electrochemical catalytic activity of obtained N-S-G catalysts for ORR.

We estimate electrochemically effective surface area of bare glassy carbon (GC) electrode, N-S-G 850 and N-S-G 1000 catalysts (Supplementary Fig. S5). The electroactive surface area of N-S-G 1000 modified electrode (0.301 cm^2) is nearly 5.90 and 3.12 times as large as that of bare GC electrode (0.051 cm^2) and N-S-G 850 modified electrode (0.096cm^2) , respectively, which enhances the charge transfer kinetics.

RDE and RRDE measurements were performed to study the electrocatalytic properties of N-S-G, N-G 1000, PAMTa/rGO and Pt/C. Fig. 6b gives linear sweep voltammograms (LSVs) of N-S-G, N-G 1000, PAMTa/rGO and Pt/C at a rotation speed of 2000 rpm in 0.1M NaOH saturated with O_2. It can be seen that, both onset potentials and limiting current densities of the obtained N-S-G catalysts are similar to that of PAMTa/rGO in the temperature range of 600-850 ℃. After pyrolysing at 1000 ℃, however, N-S-G 1000 catalyst displays the most positive onset potential and the largest limiting current density compared with PAMTa/rGO and other N-S-G catalysts. Moreover, N-S-G 1000 shows more positive onset potential and half-wave potential compared with N-G 1000. The limiting current density on N-S-G 1000 is nearly twice as large as that on N-G 1000. Therefore, the superior catalytic activity of N-S-G 1000 for ORR should be ascribed to a synergistic effect between N and S. The onset potential and half-wave potential of N-S-G 1000 is comparable with that of Pt/C. It is worth noting that the limiting current density of

N-S-G 1000 surpasses that of Pt/C at the slightly more negative potential region (-0.28 V *vs.* SCE), which should be attributed to the more kinetically facile of N-S-G 1000 for ORR.[45]

We compare our catalyst with some recently reported similar nitrogen and sulfur co-doping materials for the ORR (see Supplementary Table S1) in alkaline media. In general, the performance of our N-S-G 1000 catalyst is comparable with, or even better than those of the previous reports in terms of the onset potential, half-wave potential and limiting current density.

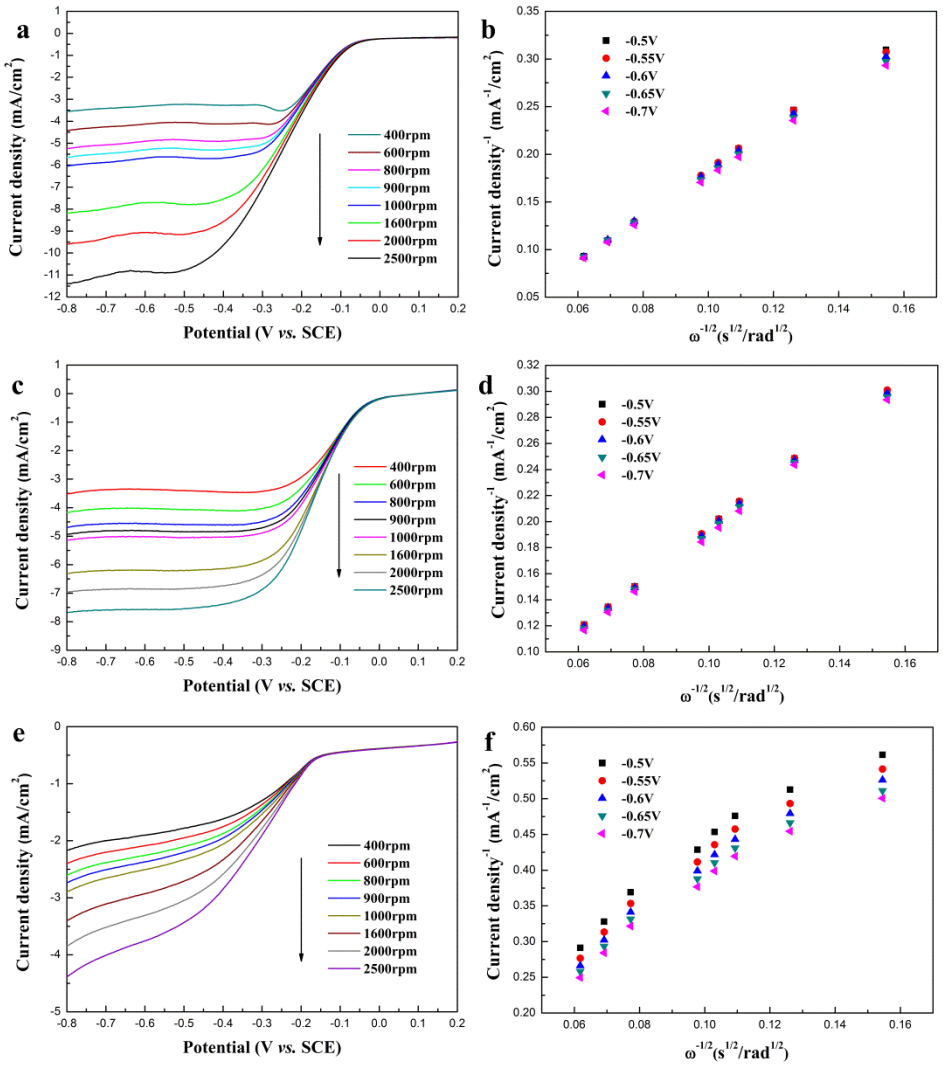

Figure 7. LSVs for ORR on (a) N-S-G 1000, (c) Pt/C and (e) PAMTa/rGO in O_2-saturated 0.1 M NaOH under different rotation speeds at a scan rate of 10 mV s^{-1}. The corresponding K-L plots for (b) N-S-G 1000, (d) Pt/C and (f) PAMTa/rGO at fixed potentials of -0.5, -0.55, -0.6, -0.65 and -0.7 V *vs.* SCE, respectively.

Fig. 7a shows the LSVs of N-S-G 1000 at different rotation speeds from 400 to 2500 rpm in 0.1 M NaOH saturated with O_2. For comparison, LSVs of Pt/C and PAMTa/rGO were also measured under the same conditions (Fig. 7c and e). Obviously, the limiting current densities of these catalysts increase by an increase in rotation speed. To further gain better insight into the electron transfer process for ORR on each sample, the Koutecky-Levich (K-L) plots were obtained for these catalysts at reaction potentials from -0.5 to -0.7 V *vs.* SCE based on LSVs at various rotation speeds (Fig. 7b, d and f). The Koutechy-Levivh (K-L) equation is given as follows:

$$\frac{1}{J} = \frac{1}{J_K} + \frac{1}{J_L} = \frac{1}{NFKC_0} + \frac{1}{B\omega^{1/2}} \quad (1)$$

$$B = 0.62nFC_0(D_0)^{2/3}\upsilon^{-1/6} \quad (2)$$

where J represents the measured current density, J_K and J_L denote the kinetic and diffusion-limiting current densities, ω is the angular velocity of the disk ($\omega = 2\pi N$, N is the linear rotation speed), n is the overall number of electrons transferred in oxygen reduction, F is the Faraday constant (F = 96485 C mol^{-1}), C_0 is the bulk concentration of O_2 (1.2×10^{-6}mol cm^{-3}), D_0 is the diffusion coefficient of O_2 in 0.1 M KOH (1.9×10^{-5} cm^2 s^{-1}), v is the kinematic viscosity of the electrolyte (0.01 cm^2 s^{-1}), and K is the electron transfer rate constant.

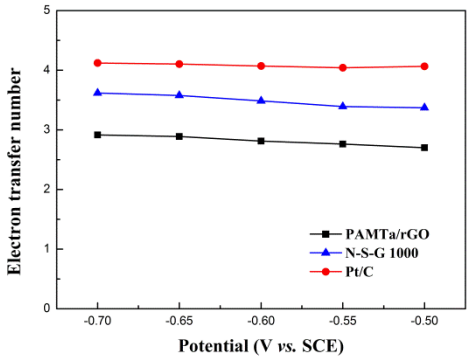

Figure 8. Electron transfer number of PAMTa/rGO, N-S-G 1000 and Pt/C at fixed potentials of -0.5, -0.55, -0.6, -0.65 and -0.7 V *vs*. SCE, respectively.

As represented in Fig. 7b, d and f, the relevant K-L plots (J^{-1} versus $\omega^{-1/2}$) for various samples exhibit a good linear relation, and their slopes remain unchanged over the potentials ranging from -0.5 to -0.7 V *vs*. SCE, which indicates that the electron transfer number at different potentials is similar. The electron transfer number of PAMTa/rGO, Pt/C and N-S-G 1000 is illustrated in Fig. 8. Pt/C displays a direct four-electron process for ORR. The electron transfer number of N-S-G 1000 is close to 3.6 at potentials ranging from -0.5 to -0.7 V *vs*. SCE, suggesting that the ORR process is mainly proceeded via a $4e^-$ pathway.[41] However, the electrons transferred number of PAMTa/rGO is less than 3, demonstrating a two-electron reduction pathway in the incomplete O_2 reduction to the peroxide anion (HO_2^-).[3]

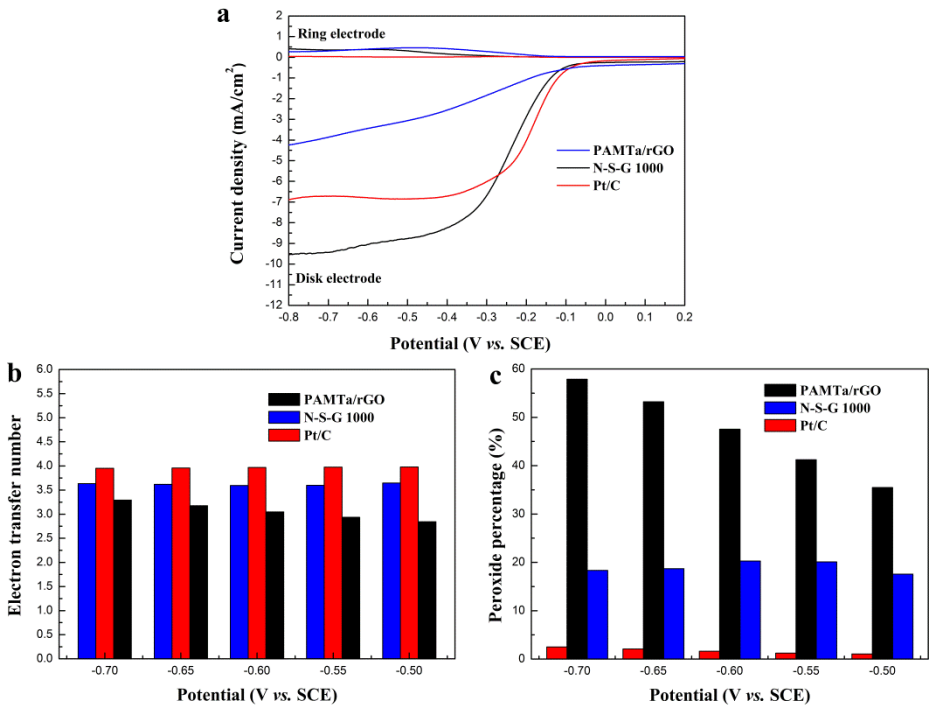

Figure 9. (a) Rotating ring disk electrode (RRDE) measurement of PAMTa/rGO, N-S-G 1000 and Pt/C in O_2-saturated 0.1 M NaOH at a scan rate of 10 mV s^{-1} with a rotation speed of 2000 rpm. (b) Electron transfer number of PAMTa/rGO, N-S-G 1000 and Pt/C at fixed potentials of -0.5, -0.55, -0.6, -0.65 and -0.7 V *vs*. SCE, respectively. (c) Hydrogen peroxide percentage of PAMTa/rGO, N-S-G 1000 and Pt/C at fixed potentials of -0.5, -0.55, -0.6, -0.65 and -0.7 V *vs.* SCE, respectively.

In order to further confirm the ORR mechanism of our catalysts for ORR, RRDE measurements were used to detect the formation of hydrogen peroxide species, which produced during ORR process at the disk electrode can be monitored by the ring electrode. The percentage of hydrogen peroxide ion and the electron transfer number can be calculated by the equations below:

$$n = \frac{4I_D}{I_D + I_R / N} \quad (3)$$

$$\%HO_2^- = \frac{200 \times I_R / N}{I_D + I_R / N} \qquad (4)$$

Where I_D is the disk current, I_R is the ring current, and N is the current collection efficiency of the Pt ring. Collection efficiency (N = 0.37) of the ring electrode is calibrated by a $K_3Fe(CN)_6$ redox reaction in N_2-saturated 0.1 M NaOH solution.

Fig. 9a shows the disk and ring current density for PAMTa/rGO, N-S-G 1000 and Pt/C catalysts in O_2-saturated 0.1 M NaOH solution. Fig. 9b and c present the electron transfer number and the percentage of HO_2^- generated at different potentials on PAMTa/rGO, N-S-G 1000 and Pt/C. As shown in Fig. 9b and c, the percentage of hydrogen peroxide ion produced by N-S-G 1000 is varied from 17.5 to 20.2 %. The electron transfer number calculated is in the range of 3.59-3.63, which is in agreement with the results calculated from K-L equation.

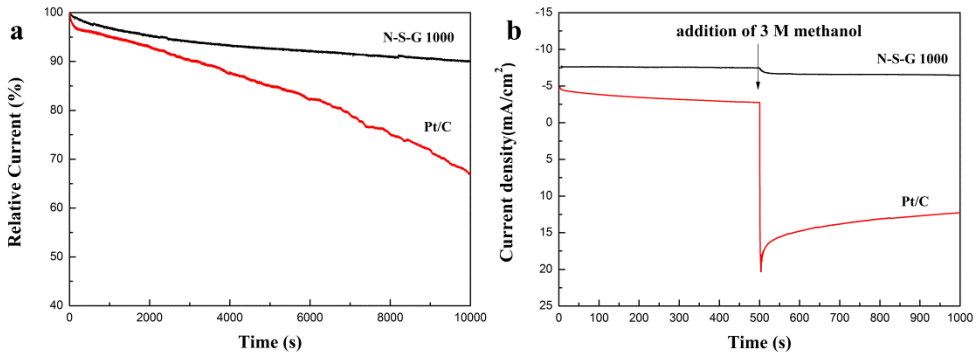

Figure 10. (a) Stability evaluation of N-S-G 1000 and Pt/C for 10000 s in an O_2-saturated 0.1 M NaOH solution at -0.3V *vs*. SCE with a rotation speed of 1600 rpm. (b) Current-time (*i-t*) chronoamperometric responses for ORR at -0.3 V *vs*. SCE in an O_2-saturated 0.1 M NaOH solution at Pt/C and N-S-G 1000 modified electrode followed by adding 3 M methanol at 500 s, which is marked with an arrow.

In addition, the stability and tolerance to methanol crossover for N-S-G 1000 and Pt/C was evaluated by current-time chronoamperometric measurements with constant potential set at -0.3V*vs*. SCE and a rotation speed of 1600 rpm in 0.1 M NaOH solution saturated with O_2. Fig. 10a displays the stabilitytest results for N-S-G 1000 and Pt/C. The current attenuation loss on Pt/C catalyst is around 33.15 % after a chronoamperometric tests for 10000 s, while N-S-G 1000 retains 89.93 % of its initial current under the same conditions. The results suggest that N-S-G 1000 catalyst possesses a significantly better stability than Pt/C.

In order to investigate the selectivity of N-S-G1000 and Pt/C, methanol was introduced at 500 s to perturb the electrodes in chronoamperometric tests. As shown in Fig. 10b, there is a strong amperometric response for Pt/C after adding methanol into the solution, while the current of N-S-G 1000 remains almost unchanged. The above results indicate that N-S-G 1000 has good selectivity for ORR.

Previous studies showed that graphitic-N can exist in any parts of graphene layers, while pyridinic-N and pyrrolic-N only locate at the edge and defect sites of graphene layers.[25, 41] Furthermore, graphitic-N possesses much higher catalytic activity than pyridinic-N and pyrrolic-N for ORR.[43, 46-47] Thiophene-S, same with pyrrolic-N, only exists at edge and defect sites of graphene layers, but thiophene-type sulfur bonding should be more effective than pyridinic-N and pyrrolic-N in ORR.[29] For the fabricated N-S-G 1000 catalyst, the atomic percentage of N and S is only 0.89 % and 0.34 %, respectively. However, most of N and S exist in the form of graphitic-N (74.6 %) and thiophene-S (90.2 %). Therefore, the

excellent catalytic activity of N-S-G 1000 catalyst for ORR should be ascribed to high electroactive surface area, more active sites of high-efficient graphitic-N and thiophene-S, as well as the synergistic effect between graphitic-N and thiophene-S.[41]

4. Conclusion

In summary, we obtained a novel N and S co-doped graphene catalyst for ORR by a one-step pyrolysis approach of GO-supported PAMTa composite. In all pyrolysing samples, N-S-G 1000 displays excellent catalytic activity in terms of more positive onset potential, half-wave potential and higher kinetic limiting current density. What is more, N-S-G 1000 catalyst possesses prominent ORR catalytic activity, excellent methanol tolerance, nearly a four-electron pathway, higher limiting current density and better stability than commercial Pt/C in alkaline medium, which should be due to high electroactive surface area, more active sites of graphitic-N and thiophene-S, as well as the synergistic effect between graphitic-N and thiophene-S. Based on our experimental results, designing N and S co-doped graphene with optimal activity and durability for ORR, may hold great promise for application in fuel cells and metal-air batteries.

Acknowledgements

This research has been financed by the National Natural Science Foundation of China (No. 21273024) and Natural Science Foundation of Jilin Province, China (No. 201215135).

References

1. H. B. Li, W. J. Kang, L. Wang, Q. L. Yue, S. L. Xu, H. S. Wang and J. F. Liu, *Carbon*, 2013, **54**, 249-257.
2. Steele, C. Brian and A. Heinzel, *Nature*, 2001, **414**, 345-352.
3. G. J. Lv, L. L. Cui, Y. Y. Wu, Y. Liu, T. Pu and X. Q. He, *Phys. Chem. Chem. Phys.*, 2013, **15**, 13093-13100.
4. M. R. Gao, Y. F. Xu, J. Jiang and S. H.Yu, *Chem. Soc. Rev.*, 2013,**42**, 2986.
5. J. P. Paraknowitsch, A. Thomas, *Energy Environ. Sci.*, 2013, **6**, 2839-2855.
6. D. S. Geng, Y. Chen, Y. G. Chen, Y. L. Li, R. Y. Li, X. L. Sun, S. Y. Ye and S. Knights, *Energy Environ. Sci.*, 2011, **4**, 760-764.
7. D. S. Yu, Y. H. Xue and L. M. Dai, *J. Phys. Chem. Lett.*, 2012, **3**, 2863-2870.
8. Y. Zheng, Y. Jiao, J. Chen, J. Liu, J. Liang, A. J. Du, W. M. Zhang, Z. H. Zhu, S. C. Smith, M. Jaroniec, G. Q. Lu and S. Z. Qiao, *J. Am. Chem. Soc.*, 2011, **133**, 20116-20119.
9. X. Yuan, X. Zeng, H. J. Zhang, Z. F. Ma and C. Y. Wang, *J. Am. Chem. Soc.*, 2010, **132**, 1754-1755.
10. M. Jahan, Q. L. Bao and K. P. Loh, *J. Am. Chem. Soc.*, 2012, **134**, 6707-6713.
11. Y. Y. Jiang, Y. Z. Lu, X. Y. Lv, D. X. Han, Q. X. Zhang, L. Niu and W. Chen, *ACS Catal.*,2013, **3**, 1263-1271.
12. Y. Zheng, Y. Jiao, L. Ge, M. Jaroniec and S. Z. Qiao, *Angew. Chem. Int. Ed.*, 2013, **52**, 3110-3116.
13. S. Mao, Z. H. Wen, T. Z. Huang, Y. Hou and J. H. Chen, *Energy Environ. Sci.*, 2014, **7**, 609-616.

14. T. Fujigaya and N. Nakashima, *Adv. Mater.*, 2013, **25**, 1666-1681.

15. T. Y. Huang, J. H. Huang, H. Y. Wei, K. C. Ho and C. W. Chu, *Biosens. Bioelectron.*, 2013,**43**, 173-179.

16. X. Huang, X. Y. Qi, F. Boey and H. Zhang, *Chem. Soc. Rev.*, 2012, **41**, 666-686.

17. J. S. Lee, K. Jo, T. Lee, T. Yun and J. Cho, *J. Mater. Chem. A*, 2013, **1**, 9603-9607.

18. Y. Q. Zhao, D. D. Zhao, P. Y. Tang, Y. M. Wang, C. L. Xu, H. L. Li Y. Q. Zhao , D. D. Zhao, P. Y. Tang, Y. M. Wang, C. L. Xu and H. L. Li, *Mater.* Lett., 2012, **76**, 127-130.

19. T. Qian, C. F. Yu, S. S. Wu and J. Shen, *Biosens. Bioelectron.*, 2013, **50**, 157-160.

20. G. Y. Chen, S. R. Bare and T. E. Mallouk, *J. Electrochem. Soc.*, 2002, **149**, A1092-A1099.

21. V. Neburchilov, H. J. Wang, J. J. Martin and W. Qu, *J. Power Sources*, 2010,**195**, 1271-1291.

22. J. Liang, X. Du, C. Gibson, X. W. Du and S. Z. Qiao, *Adv. Mater.*, 2013, **25**, 6226-6231.

23. Z. Y. Lin, G. H. Waller, Y. Liu, M. L. Liu and C. P. Wong, *Carbon*, 2013,**53**, 130-136.

24. Z. H. Sheng, H. L. Gao, W. J. Bao, F. B. Wang and X. H. Xia, *J. Mater. Chem.*, 2012, **22**, 390-395.

25. S. B. Yang, L. J. Zhi, K. Tang, X. L. Feng, J. Maier and K. Müllen, *Adv. Funct. Mater.*, 2012, **22**, 3634-3640.

26. R. Silva, D. Voiry, M. Chhowalla and T. Asefa, *J. Am. Chem. Soc.*, 2013, **135**, 7823-7826.

27. W. Ding, Z. D. Wei, S. G. Chen, X. Q. Qi, T. Yang, J. S. Hu, D. Wang, L. J. Wan, S. F. Alvi and L. Li, *Angew. Chem. Int. Ed.*, 2013, **52**, 11755-11759.

28. H. W. Liang, W. Wei, Z. S. Wu, X. L. Feng and K. Müllen, *J. Am. Chem. Soc.*, 2013, **135**, 16002-16005.

29. J. E. Park, Y. J. Jang, Y. J. Kim, M. S. Song, S. Yoon and D. H. Kim, *Phys. Chem. Chem. Phys.*, 2014, **16**, 103-109.

30. C. Z. Zhang, N. Mahmood, H. Yin, F. Liu and Y. L. Hou, *Adv. Mater.*, 2013, **25**, 4932-4937.

31. M. Latorre-Sánchez, A. Primo and H. García, *Angew. Chem. Int. Ed.*, 2013, **52**, 11813-11816.

32. S. Y. Wang, L. P. Zhang, Z. H. Xia, A. Roy and D. W. Chang, J. B. Baek, *Angew. Chem. Int. Ed.*, 2012, **51**, 4209-4212.

33. J. Liu , X. J. Sun , P. Song , Y. W. Zhang , W. Xing and W. L. Xu, *Adv. Mater.*, 2013, **25**, 6879-6883.

34. L. T. Qu, Y. Liu, J. B. Baek and L. Dai, *ACS Nano*, 2010, **4**, 1321-1326.

35. Z. H. Sheng, L. Shao, J. J. Chen, W. J. Bao, F. B. Wang and X. H. Xia, *ACS Nano*, 2011, **5**, 4350-4358.

36. Z. Y. Lin, G. H. Waller, Y. Liu, M. L. Liu and C. P. Wong, *Nano Energy*, 2013, **2**, 241-248.

37. S. Jiang, C. Z. Zhu and S. J. Dong, *J. Mater. Chem. A*, 2013, **1**, 3593-3599.

38. Y. Q. Chang, F. Hong, C. X. He, Q. L. Zhang and J. H. Liu, *Adv. Mater.*, 2013, **25**, 4794.

39. C. Z. Zhu and S. J. Dong, *Nanoscale*, 2013, **5**, 1753-1767.

40. Y. Z. Su, Y. Zhang, X. D. Zhuang, S. Li, D. Q. Wu, F. Zhang and X. L. Feng, *Carbon*, 2013, **62**, 296-301.

41. J. Liang, Y. Jiao, M. Jaroniec and S. Z. Qiao, Angew. Chem. Int. Ed., 2012, **51**, 11496-11500.

42. G. X. Wang, X P. Shen, B. Wang, J. Yao and J. Park, *Carbon*, 2009, **47**, 1359-1364.

43. L. F. Lai, J. R. Potts, D. Zhan, L. Wang, C. K. Poh, C. Tang, H. Gong, Z. X. Shen, J. Y. LinandR. S. Ruoff, *Energy. Environ. Sci.*, 2012, **5**, 7936-7942.

44. Z. Yang, Z. Yao, G. F. Li, G. Y. Fang, H. G. Nie, Z. Liu, X. M. Zhou , X. A. ChenandS. M. Huang, *ACS Nano*, 2012, **6**, 205-211.

45. Z. J. Jiang, Z. Q. Jiang and W. H. Chen. *J. Power Sources*, 2014, **251**:55-65.

46. E. J. Biddinger and U. S. Ozkan, *J. Phys. Chem. C*, 2010, **114**, 15306-15314.

47. Y. Zheng, J. Liu, J. Liang, M. Jaroniec and S. Z. Qiao, *Energ. Environ. Sci.*, 2012, **5**, 6717-6731.